

CHANDRA OBSERVATIONS OF GALAXY CLUSTER A2218

MARIE E. MACHACEK,¹ MARK W. BAUTZ, AND CLAUDE CANIZARES

Center for Space Research, Massachusetts Institute of Technology, 70 Vassar Street, Building 37, Cambridge, MA 02139

AND

GORDON P. GARMIRE

Pennsylvania State University, Department of Astronomy and Astrophysics, 525 Davey Laboratory, University Park, PA 16802

Received 2001 August 31; accepted 2001 November 7

ABSTRACT

We present results from two observations (combined exposure of ~ 17 ks) of galaxy cluster A2218 using the Advanced CCD Imaging Spectrometer on board the *Chandra X-Ray Observatory* that were taken on 1999 October 19. Using a Raymond-Smith single-temperature plasma model corrected for galactic absorption, we find a mean cluster temperature of $kT = 6.9 \pm 0.5$ keV, metallicity of 0.20 ± 0.13 (errors are 90% CL), and a rest-frame luminosity in the 2–10 keV energy band of 6.2×10^{44} ergs s^{−1} within a 5′.1 aperture in a Λ cold dark matter cosmology (Λ CDM) with $H_0 = 65$ km s^{−1} Mpc^{−1}. The brightness distribution within 4′.2 of the cluster center is well fitted by a simple spherical beta model with core radius of 66′.4 and $\beta = 0.705$. High-resolution *Chandra* data of the inner 2′ of the cluster show the X-ray brightness centroid displaced $\sim 22''$ from the dominant cD galaxy and the presence of azimuthally asymmetric temperature variations along the direction of the cluster mass elongation. X-ray and weak lensing mass estimates are in good agreement for the outer parts ($r > 200 h^{-1}$) of the cluster; however, in the core the observed temperature distribution cannot reconcile the X-ray and strong lensing mass estimates in any model in which the intracluster gas is in thermal hydrostatic equilibrium. Our X-ray data are consistent with a scenario in which A2218 is not in hydrostatic equilibrium because of recent merger activity that has produced significant nonthermal pressure in the core and substructure along the line of sight; each of these phenomena probably contributes to the difference between lensing and X-ray core mass estimates.

Subject headings: galaxies: clusters: general — galaxies: clusters: individual (A2218) — intergalactic medium — X-rays: galaxies: clusters

1. INTRODUCTION

Galaxy clusters are the largest gravitationally bound systems known. Within our current hierarchical picture of structure formation, they form quite late at the knots and intersections of overdense filaments through mergers of subcluster-sized gas clouds and galaxies, and these mergers may well be, in many cases, ongoing. Investigations of the mass distributions and merger dynamics of these clusters provide insight into the amount and nature of the dark matter expected to dominate the gravitational potential and may elucidate the complex gas dynamics and energy transfer mechanisms of the merger process itself. After the internal structure and dynamical state of the cluster are well understood, they can be used to deduce other cosmological parameters. For example, a comparison of the X-ray surface brightness to the reduction in the cosmic microwave background (CMB) due to inverse Compton scattering of CMB photons off the hot intracluster gas can be used to infer the value of the Hubble parameter H_0 (Sunyaev & Zel'dovich 1972, 1980; Birkinshaw & Hughes 1994). Thus, galaxy clusters serve as important laboratories to constrain and expand on cosmological models of structure formation.

Fortunately, the large mass and relatively low redshift of galaxy clusters also give us the means to unravel the mystery of their complex dynamics. Observations of the velocity dispersions of galaxies probe the cluster gravitational potential in which they move. Details of the galaxy

velocity distribution may signal recent galaxy-galaxy interactions and merging activity. In many of these clusters gravitational lensing, both strong and weak, provides a direct measure of the total projected mass, gas plus dark matter, within the cluster. Strong lensing measures the total projected mass at small radii, i.e., within the critical radius of the lensed arc, while weak lensing is more sensitive to the mass distribution out to larger radii. Thermal X-ray emission from the hot intracluster gas measures directly the gas density and temperature distributions within the cluster. This hot gas is confined by and expected to trace the underlying three-dimensional gravitational potential. Under the assumption of thermal hydrostatic equilibrium, these gas properties may be used to infer the cluster total mass distribution. A comparison of X-ray to lensing projected total mass poses an important check on the validity of this assumption. For most dynamically relaxed clusters, where the cluster contains a single dominant galaxy at its center, agreement is quite good. The X-ray surface brightness contours tend to be smooth and roughly spherical. The mass centroids determined by lensing and X-ray analyses coincide with each other, the peak of the X-ray emission, and also the position of the dominant galaxy (see, e.g., Allen 1998). However, for clusters that appear more active dynamically, the lensing mass may be as much as a factor of 2–3 above the X-ray mass estimates (Miralda-Escude & Babul 1995; Allen 1998). Possible explanations for such a significant disparity between the X-ray and lensing masses seem linked to the presence of recent merging activity within the cluster and include the possibility of complicated cluster temperature profiles (Makino 1996; Cannon,

¹ On leave from Department of Physics, Northeastern University, Boston, MA 02115.

Ponman, & Hobbs 1999), the departure of the cluster from thermal hydrostatic equilibrium such that there is significant nonthermal pressure support in the cluster gas (Loeb & Mao 1994; Miralda-Escude & Babul 1995), or clumpiness along the line of sight (Bartelmann & Steinmetz 1996).

A2218 is a prototype galaxy cluster in this latter category. It is an Abell richness class 4 cluster at redshift $z = 0.175$ with an intricate array of gravitationally lensed arcs and more than 100 arclets (Pello et al. 1992). Its measured velocity dispersion, 1370^{+160}_{-120} km s⁻¹, is high for its X-ray temperature (LeBorgne, Pello, & Sanahuja 1992). Previous X-ray observations find mean cluster temperatures between 6.7 (McHardy et al. 1990; Cannon et al. 1999) and 7.2 keV (Mushotzky & Loewenstein 1997; Allen 1998), metallicities close to 0.2, and a 2–10 keV X-ray luminosity in a flat, standard cold dark matter cosmology (SCDM; $H_0 = 50$ km s⁻¹ Mpc⁻¹, $\Omega_m = 1$) of $\sim 10^{45}$ ergs s⁻¹ (David et al. 1993; Allen 1998). There is evidence from *ASCA* data of a temperature decline for radii greater than a few arcminutes (Loewenstein 1997). Observations in both the optical and the X-ray suggest recent dynamical activity. Natarayan & Kneib (1996) found velocity dispersion profiles for galaxies in the cluster core that were inconsistent with equilibrium. In a recent photometric study of 49 galaxies in A2218, Ziegler et al. (2001) find that older galaxies, as determined by their stellar populations, are not concentrated near the core but are well mixed throughout the cluster. Such mixing is expected within a few dynamical times after a major merger event. They also find one galaxy (1662) in the core whose stars have an unusually high velocity dispersion, suggesting that it may have been tidally stripped. Gravitational lensing analyses of the arcs and arclets in A2218 require multiply peaked total mass concentrations within the cluster (Kneib et al. 1996), while a nonparametric mass reconstruction using both strong and weak lensing data shows that the mass concentrations are offset from the light, i.e., the dominant cD and second brightest elliptical galaxies, respectively (AbdelSalam, Saha, & Williams, 1998). While early X-ray observations appeared to place the peak X-ray emission at the location of the dominant cD galaxy (Birkinshaw & Hughes 1994; Squires et al. 1996), more recent analyses using higher resolution *ROSAT* data confirm a more complex picture of the cluster core. Markevitch (1997) found evidence in Gaussian-smoothed *ROSAT* HRI data of multiple X-ray peaks significantly displaced from the cD galaxy, while Allen (1998) found, using an iterative procedure, that the centroid of the X-ray emission was also displaced from the cD galaxy toward the direction of the second brightest elliptical galaxy. Improvements in the X-ray data and lensing analyses have failed, however, to reconcile the discrepancy of at least a factor 2 between the projected mass distributions inferred by these two techniques.

In this paper we present results of two observations (~ 11 and ~ 6 ks) of A2218 by the *Chandra X-Ray Observatory*. In § 2 we detail the observations and the data reduction and processing procedures. In § 3 we present our main results. We first discuss our measurements of the global properties of the cluster. We then exploit the unprecedented spatial resolution of *Chandra* to focus on the structure of the cluster core. Finally, we determine the projected total mass distribution implied by the X-ray data and compare it to the lensing results. In § 4 we interpret these findings in terms of past merging activity within the cluster core, and we

summarize our results in § 5. All errors are 90% confidence limits and coordinates are J2000.0. Unless noted otherwise we state our results in the currently preferred flat, low matter density Λ CDM cosmology ($\Omega_m = 0.3$, $\Omega_\Lambda = 0.7$, $h = 0.65$) with Hubble parameter $H_0 = 100 h$ km s⁻¹ Mpc⁻¹. Thus, for the cluster redshift $z = 0.175$, 1'' corresponds to a distance scale of $2.08 h^{-1}$ kpc.

2. OBSERVATIONS AND ANALYSIS

A2218 was observed twice, for 11.4 and 5.9 ks, by the *Chandra X-Ray Observatory* on 1999 October 19. The data were obtained using the Advanced CCD Imaging Spectrometer (ACIS; Garmire et al. 1992; Bautz et al. 1998) with a focal plane temperature of -110 C throughout the observations. All four of the front-illuminated CCDs (I0–I3) in the 2×2 imaging array (ACIS-I) were active in both exposures. In addition CCD(s) S2 (S2, S3) from the 1×6 spectrometer array were active for the longer (shorter) exposure. However, the telescope pointing placed the bulk of the cluster emission on CCD I-3. Thus, in this analysis we use only data from the ACIS-I array for imaging and CCD I3 for spectral analysis. Each CCD is a 1024×1024 pixel array where each pixel subtends $0''.492 \times 0''.492$ on the sky.

The data were ground reprocessed on 2000 September 27 by the *Chandra X-Ray Center* (CXC), resulting in better quiescent background rejection, an improved aspect solution, and better modeling of instrument gain and quantum efficiency, including its position dependence within the chip. This latter modeling of quantum efficiency (non)uniformity partially corrects for the charge transfer inefficiency induced along the chip readout direction for front-illuminated CCDs believed to have been caused by exposure to low-energy protons during the passage of the telescope through the Earth's radiation belts shortly after launch (Prigozhin et al. 2000). For our data, this is particularly important not only because the ACIS-I array is front-illuminated but also because the telescope orientation placed the axis of the mass elongation of the cluster, along which we might expect important physical effects to appear, close to the readout direction of the chip. Thus, we used an earlier release of the data only to check for the qualitative consistency of our results and the efficacy of cleaning and analysis algorithms. The results presented here are based solely on the reprocessed data sets using the most recent instrumental corrections. We used throughout the CXC *Chandra* Interactive Analysis of Observations analysis suite CIAO 2.0 for the imaging analyses and the high-energy astrophysics software packages FTOOLS and XSPEC to fit spectra.

Bad pixels were removed from each observation using the CXC-provided observation-dependent bad pixel files. We checked the light curves for each observation for periods of anomalously high background (flares) and found none. Cosmic-ray contamination was minimized in the CXC-reprocessed data by rejecting *ASCA* event grades 1, 5, and 7 and applying the algorithm “acis-detect-afterglow” to remove residual flaring pixel events. Cosmic-ray-induced flaring pixels mimic point sources in the data. However, in high count rate data, the cleaning algorithm “acis-detect-afterglow” has a tendency to overclean the data, removing some signal. To check that our point-source identifications are robust, we compared the results from analyses in which the flaring pixels were identified by directly scanning the event list for each source candidate found in data not cleaned with “acis-detect-afterglow” to results from the

same observation after the cleaning algorithm was applied. We found that for our data sets “acis-detect-afterglow” worked well, causing no significant loss of signal while removing all but three events of the flaring pixel contamination. Thus, no further cleaning of the reprocessed data sets was required. We used CIAO 2.0 tools to combine the data sets for imaging and point-source identifications. For spectral analyses, we analyzed the data sets jointly rather than combining the sets since the instrument files needed are observation-dependent.

In Figure 1 we present a broadband (0.3–7 keV), exposure-corrected, adaptively smoothed *Chandra*/ACIS-I image of A2218. The data have been binned by four such that an image pixel subtends 1.96 arcsec^2 on the sky and adaptively smoothed using the CIAO tool “csmooth.” Telescope vignetting and spatial efficiency variations have been corrected by means of an exposure map for the combined, two-observation data set. The exposure map was generated using standard CIAO tools, assuming the best-fit model spectral energy distribution for the integrated cluster emission (see § 3.1). We see that with *Chandra*’s high spatial resolution we resolve a large number of X-ray point sources within the field, i.e., ~ 8.4 from the location of the cluster

center, where cluster emission is also expected to be significant.

In order to check the *Chandra* astrometry we ran the CIAO wavelet point-source detection algorithm “wavdetect” (Dobrzycki et al. 1999; Freeman et al. 2002) on the broadband (0.3–7 keV) image of the cluster field. With a “wavdetect” significance parameter set to 10^{-7} , the expected number of false detections for this field is 0.4, while we identified 52 point-source candidates. A detailed discussion of these sources will be presented elsewhere. We compared our source list with the optical USNO-A2.0 catalog (Monet 1998). Using a correlation radius of $0''.5$, we found four matches within a $14'$ radius of the ACIS-I center. The cumulative probability of a single random association between these data is 0.014; the probability that all four matches occurred by chance is 1.6×10^{-9} . Thus, the astrometry is good to within the nominal $0''.5$ without further adjustments. All X-ray point-source candidates were removed from the data for the analyses of the galaxy cluster diffuse emission presented here.

Background rates significantly affect model fitting of the surface brightness profiles and spectral analyses and, thus, estimates of the cluster mass. *ROSAT* images of A2218

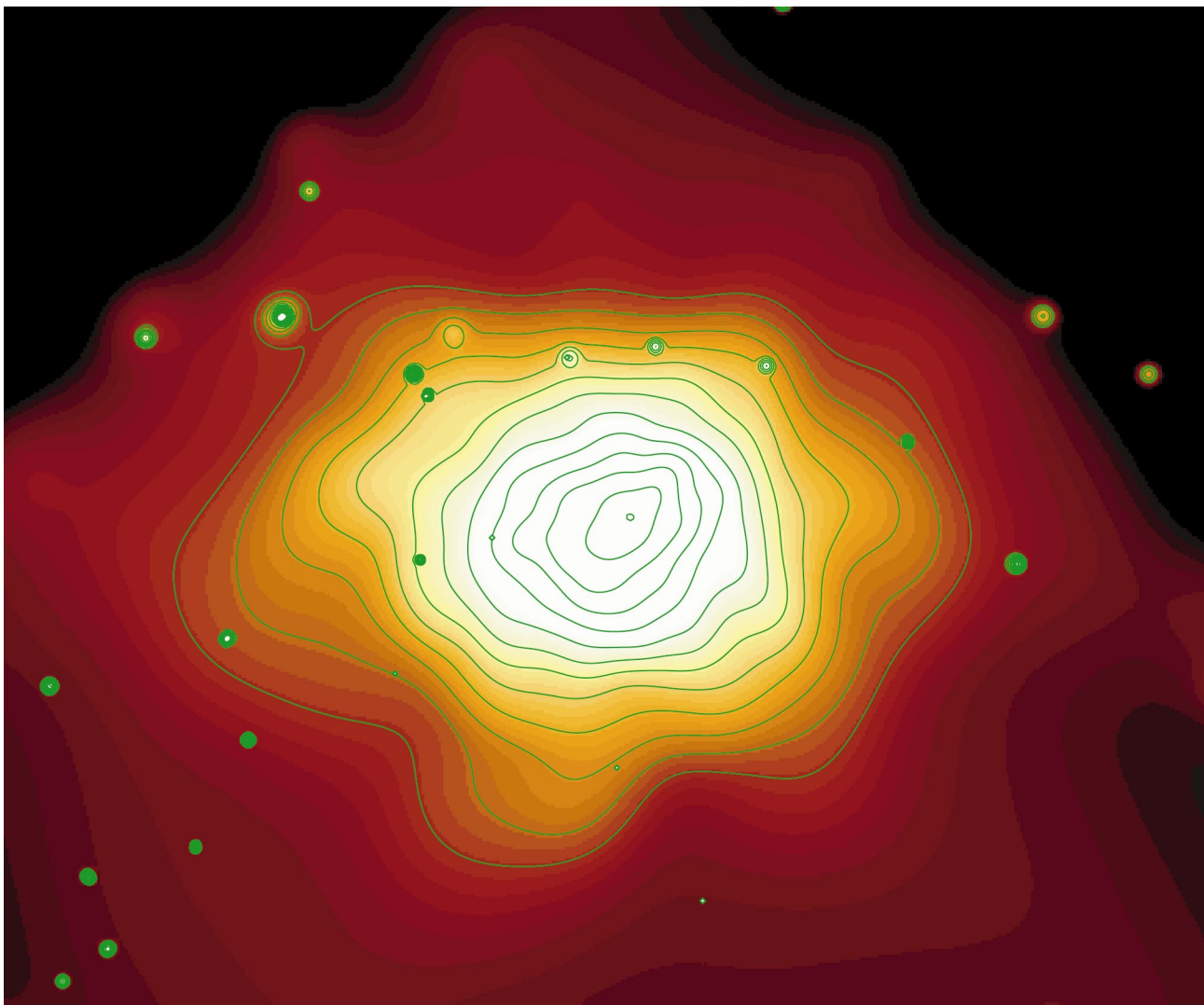


FIG. 1.—Adaptively smoothed, exposure-corrected, broadband (0.3–7 keV) *Chandra* image of A2218. The field is $14'.2 \times 11'.87$ with north up and east to the left. Contours range in steps of $\sqrt{2}$ from 0.0156 counts arcsec^{-2} , where the lowest contour is twice the background.

show that cluster emission extends to a radius $\gtrsim 12'$ from the central cD galaxy (Cannon et al. 1999), so the ACIS-I field of view is too small to find a region in our observations without significant cluster contamination from which to measure the background rate. We use instead the blank-field background sets “acisi_B_i0123_bg_evt_060600.fits” for the imaging array and “acisi_B_i3_bg_evt_060600.fits” for CCD I-3 compiled by Markevitch (2001)² and drawn for our observations using the script “make_acisbg_CIAO2” supplied with the blank-field data. We apply the same cleaning algorithm to the data as was applied to the background sets. This results in the additional removal of low count rate periods at the beginning and end of the observations, reducing the useful exposure times to 11,408 and 5704 s, respectively. Identical spatial and energy filters are applied to source and background data so that the background normalization is set by the ratio of exposure times. We check this normalization by comparing high-energy photon (9–12 keV) counts in the data, where background is expected to dominate, to that predicted by the normalized blank-field background sets and find that they differ by 5.2%. We adopt this discrepancy as our relative uncertainty in the background level.

3. RESULTS

In this section we present the main results of our analysis. In § 3.1 we determine the mean properties of the cluster as a whole and find that we are, in general, in excellent agreement with previous work. In § 3.2 we explore the complex structure of the inner $\sim 2'$ of the cluster core. In § 3.3 we use our data to determine the total projected mass as a function of radial distance from the dominant cD galaxy and compare our results with gravitational lensing analyses of the same regions.

3.1. Mean Cluster Properties

Spectroscopy.—To investigate the mean temperature and metallicity of the cluster, we extract spectra for each observation from events, after point sources are removed, that lie both on CCD I-3 and within a circular aperture with radius 5.1 (corresponding to a radius of $0.64 h^{-1}$ Mpc) centered on the peak of the broadband X-ray emission. We group the data to require a minimum of 20 counts per spectral bin. We then jointly fit the spectral data from both observations with a single-temperature Raymond-Smith plasma model (Raymond & Smith 1977) corrected for galactic absorption using Wisconsin photoelectric cross sections (Morrison & McCammon 1983). For energies below 0.7 keV, the uncertainties in the currently available ACIS-I response functions are relatively large, while for energies above 9 keV, the data become background-dominated. Thus, we restrict our fit to the 0.7–9 keV energy band resulting in a total sample size of 12,217 (6169) events in the 11.4 (5.7) ks exposure. Once the redshift of the source is fixed, an absorbed Raymond-Smith model has, in principle, four free parameters: the absorbing column density, temperature, metallicity, and normalization. We find that fitting all parameters simultaneously results in an anomalously high absorbing column density, with depressed temperature and increased metal abundance, over that determined by a fit with similar reduced χ^2

in which the absorption column density is fixed at its Galactic value. Mazzotta et al. (2001) determined that this fit degeneracy was due to remaining calibration uncertainties in the ACIS-I CCDs and that reliable temperatures could be obtained by fixing the absorption column from previous measurements. We also adopt this strategy freezing the absorbing column at its Galactic value of $3 \times 10^{20} \text{ cm}^{-2}$ (McHardy et al. 1990).

Our best-fit results using the blank-field background sets discussed in § 2 are summarized in Table 1. We find a mean temperature and metal abundance for A2218 of $kT = 6.9 \pm 0.5$ keV and $Z = 0.20 \pm 0.13$ (with reduced $\chi^2 = 0.993$). These results are in excellent agreement with previous measurements by McHardy (1990) using *Ginga* data, by Mushotzky & Loewenstein (1997) using an integrated *ASCA* spectrum, by Cannon et al. (1999) using combined *ASCA* Gas Imaging Spectrometer (GIS) 2 and 3 data, and by Allen (1998) using both Solid-State Imaging Spectrometer (SIS) and GIS *ASCA* data. We find the flux in the 0.7–9 keV energy to be $8.5 \times 10^{-12} \text{ ergs s}^{-1} \text{ cm}^{-2}$ for this aperture with an implied rest-frame luminosity in the 2–10 keV energy band of $6.2 \times 10^{44} \text{ ergs s}^{-1}$ ($h = 0.65$). As a final check on the sensitivity of our results to the blank-field background normalization, we increase the normalization of the background by 5.2% and 10.7% and find $kT = 6.7 \pm 0.5$ keV, $Z = 0.18 \pm 0.13$ (with reduced $\chi^2 = 1.002$) and $kT = 6.5 \pm 0.5$ keV, $Z = 0.15 \pm 0.12$ (with reduced $\chi^2 = 1.020$), respectively. As expected, increasing the background normalization lowers the fit temperatures and metal abundances, but the dependence is weak, and all results agree within their 90% confidence limits.

Imaging.—We model the surface brightness distribution integrated over the total exposure time with a simple, spherically symmetric core index (beta) model of the form

$$S_x(r) = S_{x0} \left(1 + \frac{r^2}{r_c^2} \right)^{-3\beta+1/2}, \quad (1)$$

where S_{x0} is the X-ray surface brightness in units of photon counts $\text{arcsec}^{-2} \text{ s}^{-1}$ at the distribution centroid (x_0, y_0), r is the projected radial distance from the centroid, and r_c is the core radius, each measured in arcseconds, and β is a dimensionless index. If the plasma is assumed to be isothermal, then this distribution can be inverted to infer a gas density distribution of the form

$$\rho_g(r) = \rho_{g0} \left(1 + \frac{r^2}{r_c^2} \right)^{-3\beta/2}, \quad (2)$$

where ρ_{g0} is the gas density at the center of the distribution. We select a broad energy band, 0.3–7 keV, for the analysis and choose an 8.4×8.4 field from the combined event lists for both observations (total exposure ~ 17 ks with 21,808 total counts) for the image that is centered roughly at the visual peak of the broadband emission. This region is a

TABLE 1
MEAN SPECTRAL PROPERTIES OF THE CLUSTER

Energy Band (keV)	kT (keV)	Abundance	$L_x(2-10 \text{ keV})$ (ergs s^{-1})	χ^2/dof
0.7–9	6.9 ± 0.5	0.20 ± 0.13	6.2×10^{44}	433/436

NOTE.—Using an aperture of radius 5.1 ($0.64 h^{-1}$ Mpc) on CCD I-3 assuming Galactic absorption, $3 \times 10^{20} \text{ cm}^{-2}$. Errors are 90% CL.

² Available at http://asc.harvard.edu/cal/Links/Acis/acis/Cal_prods/bkgnd/current/index.html.

compromise between the need to be big, since the beta model is sensitive to emission at larger radii, and the need to avoid the imaging array edges to eliminate spurious numerical effects from the fitting algorithm. The background is modeled as a constant taken to be the mean photon counts arcsec^{-2} for the above energy range determined from the blank-field background sets for the ACIS-I array and normalized, as before, by the ratio of exposure times. We allow the core radius r_c , index β , normalization S_{X0} , and the centroid parameters x_0 and y_0 to vary. Their best-fit values are found through minimization of the loglikelihood Cash statistic appropriate for Poisson distributed data using the CIAO tool SHERPA.

As summarized in Table 2, we find a core radius $r_c = 66''.4$ ($\pm 0''.45$), index $\beta = 0.705$ ($0.004, -0.003$), normalization $S_{X0} = 5.578(\pm 0.069) \times 10^{-5}$ counts $\text{arcsec}^{-2} \text{ s}^{-1}$, and the X-ray emission centroid located at $\alpha = 16^{\text{h}}35^{\text{m}}52^{\text{s}}.4$ ($\pm 0''.89$), $\delta = +66^{\circ}12'34''.4$ ($\pm 0''.84$). The intervals in parentheses represent 90% confidence limits. If we relax our assumption of spherical symmetry and fit the region with an elliptical beta model instead, the ellipticity is small, 0.179 (± 0.009), implying an axis ratio of 0.82 , close to spherical and in agreement with previous work (Siddiqui 1995), with no significant change in the center of the distribution or β . The major axis of the large field beta model fit is oriented at an angle $4''.6 \pm 2''.8$ north of west. We note that this differs considerably from the direction of the orientation axis of the inner X-ray contours and mass elongation in the cluster core ($\sim 40^\circ$ north of west as seen in Figs. 1, 2, and 4). Thus, there is considerable isophotal twisting in the inner $2'$ of the cluster. The core radius of the elliptical fit also increases to $73''.1$ ($-0''.4, 0''.6$) because of the assumed elliptical symmetry. However, in general, the deviations from spherical symmetry in the large field are small so that our use of the spherical beta model to infer the global mass distribution should be adequate. Our values for the core radius and β -index in the spherical beta model fit are consistent at the 90% confidence level with previous fits by Birkinshaw & Hughes (1994) using *Einstein* IPC and HRI data and those by Squires et al. (1996) using *ROSAT* PSPC data but are somewhat higher than the *ROSAT* HRI results ($r_c = 58''$, $\beta = 0.63$) found by Markevitch (1997). However, the 30 ks HRI exposure used by Markevitch would not have sampled well the outskirts of the cluster at radii much greater than $2'$.

More striking is the best-fit location of the X-ray emission centroid. The central dominant cD galaxy is located at $\alpha = 16^{\text{h}}35^{\text{m}}49^{\text{s}}.2$, $\delta = +66^{\circ}12'45''$ (Markevitch 1997). Thus, we find that the mean broadband X-ray emission centroid is

offset by $22'' \pm 1''.2$ ($19''$ east and $11''$ south) from the cD galaxy (see Table 2). This agrees within $5''$ with the X-ray emission centroid found using iterative methods by Allen (1998) in *ROSAT* HRI data. The offset of the X-ray emission centroid from the dominant cD galaxy is in the same direction as, although $\sim 10''$ east of, the dominant peak in the total mass distribution needed by AbdelSalam et al. (1998) in a nonparametric analysis of the weak and strong lensing data. Our measurement also agrees in magnitude with the X-ray emission peak offset from the cD galaxy found by Markevitch (1997), although our fit places the emission centroid closer to ($\lesssim 4''$ east of) the galaxy 1662 with anomalously high velocity dispersion (Ziegler et al. 2001) than to the bright face-on galaxy at the southern edge of the giant red arc. We find no evidence for lensed emission from the giant arc, which was suggested by Markevitch (1997) as one of several possible interpretations of the X-ray structure seen in the *ROSAT* HRI image.

3.2. The Central $2'$

Let us next focus on the central $\sim 2'$ of the cluster core. In Figure 2 we show exposure-corrected, adaptively smoothed X-ray images of the innermost core region of the cluster for two energy bands, $0.3\text{--}2$ keV (*upper left-hand panel*) and $2\text{--}7$ keV (*upper right-hand panel*). As in Figure 1, the data are binned by four, corrected for telescope vignetting and spatial efficiency variations by means of an exposure map, and adaptively smoothed with minimum and maximum signal-to-noise thresholds set at 3 and 5σ , respectively. Beneath each X-ray image we show the X-ray contours for that image superposed on the *Hubble Space Telescope* (*HST*) image of the same field. We denote the main peaks in the X-ray images by “S” for the soft band and “H1” for the hard band (with a second possible hard emission peak at “H2”) and superpose these locations on all of the panels. The peaks are broad with adaptively determined smoothing scales of $7''$ for the soft (S) peak and $10''$ for the hard (H1) peak. However, the images clearly show that the soft and hard emission peaks are displaced from each other. We summarize these offsets in Table 3. The peak of the soft emission lies $\sim 17''.5$ ($\sim 36 h^{-1}$ kpc) to the south and east of the cD galaxy in the direction of the mass elongation and the location of the major mass concentration found in the nonparametric treatment of strong and weak lensing by AbdelSalam et al. (1998), while the hard emission peak H1 lies $\sim 20''$ ($\sim 42 h^{-1}$ kpc) to the north and west of the soft emission peak and close to (possibly just north of) the cD galaxy. The contours in Figure 2 are smooth but distorted

TABLE 2
BETA MODEL FITS OF THE CLUSTER

FIELD	ENERGY BAND (keV)	CENTROID		r_c (arcsec)	β	S_{X0} (10^{-5} counts $\text{arcsec}^{-2} \text{ s}^{-1}$)	ϵ
		R.A.	Decl.				
Mean.....	0.3–7	16 35 52.4	66 12 34.3	66.4 ± 0.45	$0.705^{+0.004}_{-0.003}$	5.578 ± 0.069	0
Core.....	0.3–7	16 35 52.3	66 12 35.4	$73.1^{+0.6}_{-0.4}$	$0.706^{+0.003}_{-0.004}$	5.642 ± 0.069	0.18 ± 0.01
				75.1 ± 0.6	$0.774^{+0.006}_{-0.007}$	5.364 ± 0.069	0
	0.3–2	16 35 52.2	66 12 35.2	77.6 ± 0.8	$0.792^{+0.008}_{-0.007}$	3.861 ± 0.064	0
	2–7	16 35 52.3	66 12 36.1	69.8 ± 1.2	$0.737^{+0.012}_{-0.012}$	1.503 ± 0.040	0

NOTE.—The centroid of the beta model given in J2000.0 coordinates has been determined by the fit. Units of right ascension are hours, minutes, and seconds, and units of declination are degrees, arcminutes, and arcseconds. The mean (core) fields are $8''.4 \times 8''.4$ ($4''.2 \times 4''.2$) centered on the peak of the broadband emission. Other fit parameters are defined as follows: r_c is the core radius, β is the index given in eq. (1), S_{X0} is the central brightness, and ϵ is the ellipticity. Errors are 90% confidence limits. Formal errors for the centroid are $\lesssim 2''$.

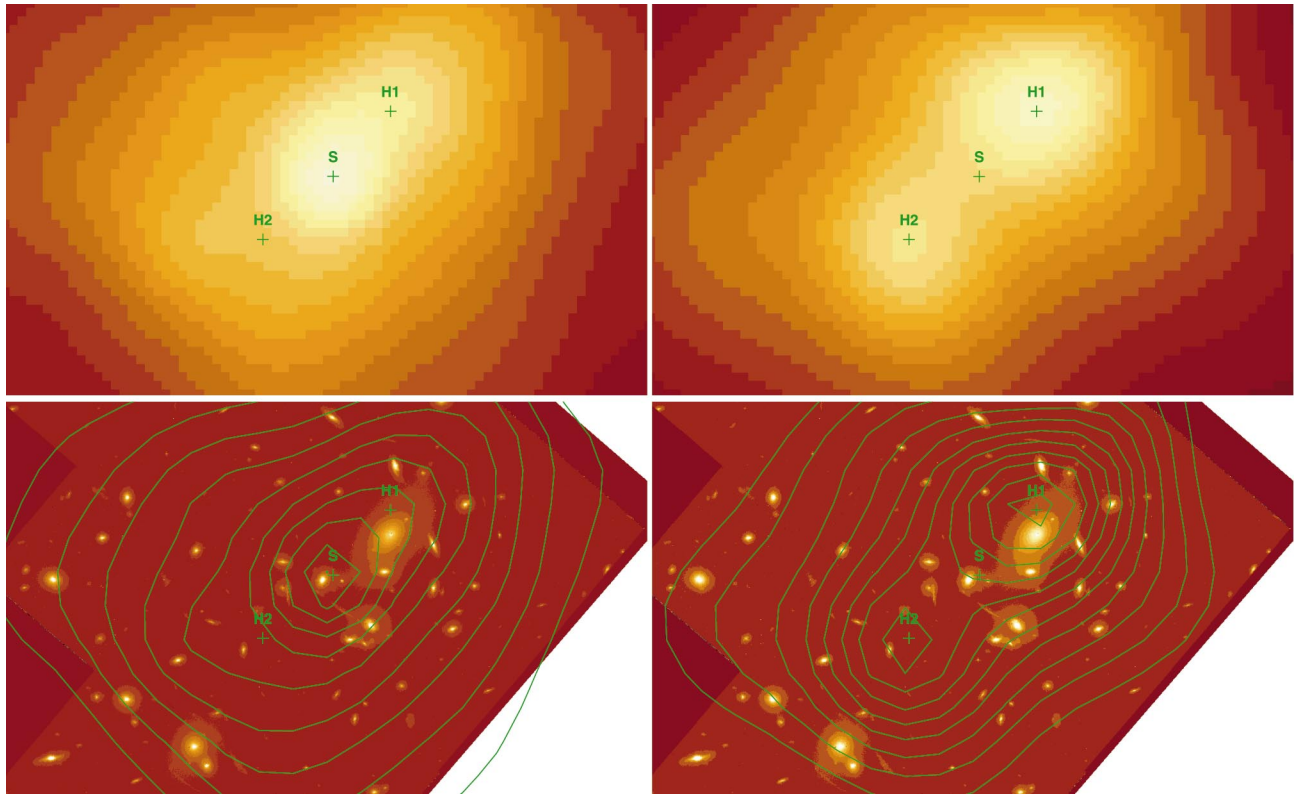


FIG. 2.—Adaptively smoothed, exposure-corrected images of soft (0.3–2 keV; *upper left*) and hard (2–7 keV; *upper right*) emission from the core of A2218. The soft (hard) peaks are denoted by S (H1, H2). In the lower left-hand (right-hand) images, contours from the soft (hard) band X-ray images are superposed on the *HST* image of the same field. The maximum contour for the soft (hard) band images corresponds to 6.06×10^{-8} (1.72×10^{-8}) photons $\text{s}^{-1} \text{cm}^{-2} \text{s}^{-1}$ and decreases linearly in intervals of 3.57×10^{-9} (0.84×10^{-9}) photons $\text{s}^{-1} \text{cm}^{-2} \text{s}^{-1}$.

and hint of possibly multi-peaked structures. The coincidence of the soft band peak with the galaxy 1662 in the optical image suggests that we may be seeing some contamination by galaxy emission. We will comment on this further in § 4. However, the general elongation of the contours along the line containing the two major mass concentrations as well as the distortions perpendicular to this axis are features caused by the intracluster gas.

In Table 2 we present results of spherical beta model plus constant background fits for hard (2–7 keV), soft (0.3–2 keV), and broadband (0.3–7 keV) emissions determined from images restricted to the central 4.2×4.2 region of the cluster. The constant background is chosen as before to be the mean background taken from the ACIS-I blank-field background sets restricted to the appropriate energy band and normalized by the ratio of exposure times. We again

allow the location of the centroid to be a free parameter in the fits to see if the energy band dependence of the peak emission shown in the images is reflected as well in a similar shift in the beta model centroids of the X-ray emission in each band. It is not. We find that the location of the best-fit centroid is remarkably stable with formal errors $\lesssim 2''$ in each case and agrees within the 90% confidence limits for each fit. Since the location of the X-ray centroid is most sensitive to emission at large radii, this is further evidence that the disturbances in the cluster are confined to the inner regions of the core. The complicated image structure is reflected in the different, and anomalously high, core radii and β indices required by the fits. This inconsistency between beta model fits to the core and fits to the global cluster was also found by Markevitch (1997) in the *ROSAT* data.

We can gain further insight into the departure of the X-ray surface brightness and thus gas density distributions from the broadband large field beta model fit by investigating the beta model residuals for this region. We smooth these residuals using a fixed two-dimensional Gaussian kernel with $\sigma = 5''$ and, in Figure 3, overlay the contours from that image on the *HST* optical mosaic of the cluster core. The residuals show a deficit of X-ray-emitting gas (*negative contours*) extending between the two major mass concentrations and directed initially perpendicular to the direction of the mass elongation. This deficit then arcs outward in a crescent-like shape around the region containing the dominant cD galaxy. There is a steep gradient from negative to positive contours just southeast of the primary mass concentration framing a large region of excess emis-

TABLE 3
OFFSETS OF THE X-RAY FEATURES FROM THE DOMINANT
cD GALAXY

Feature	Energy Band (keV)	Offset (arcsec)	Offset (h^{-1} kpc)
Centroid	0.3–7	–21.9	–45.6
Peak	0.3–7	–9.5	–19.8
Peak (S)	0.3–2	–17.5	–36.4
Peak (H1)	2–7	4.5	9.4
Peak (H2)	2–7	–39.2	–81.6

NOTE.—Negative (positive) offsets are to the south and east (north and west), respectively. Peak positions are taken from adaptively smoothed images.

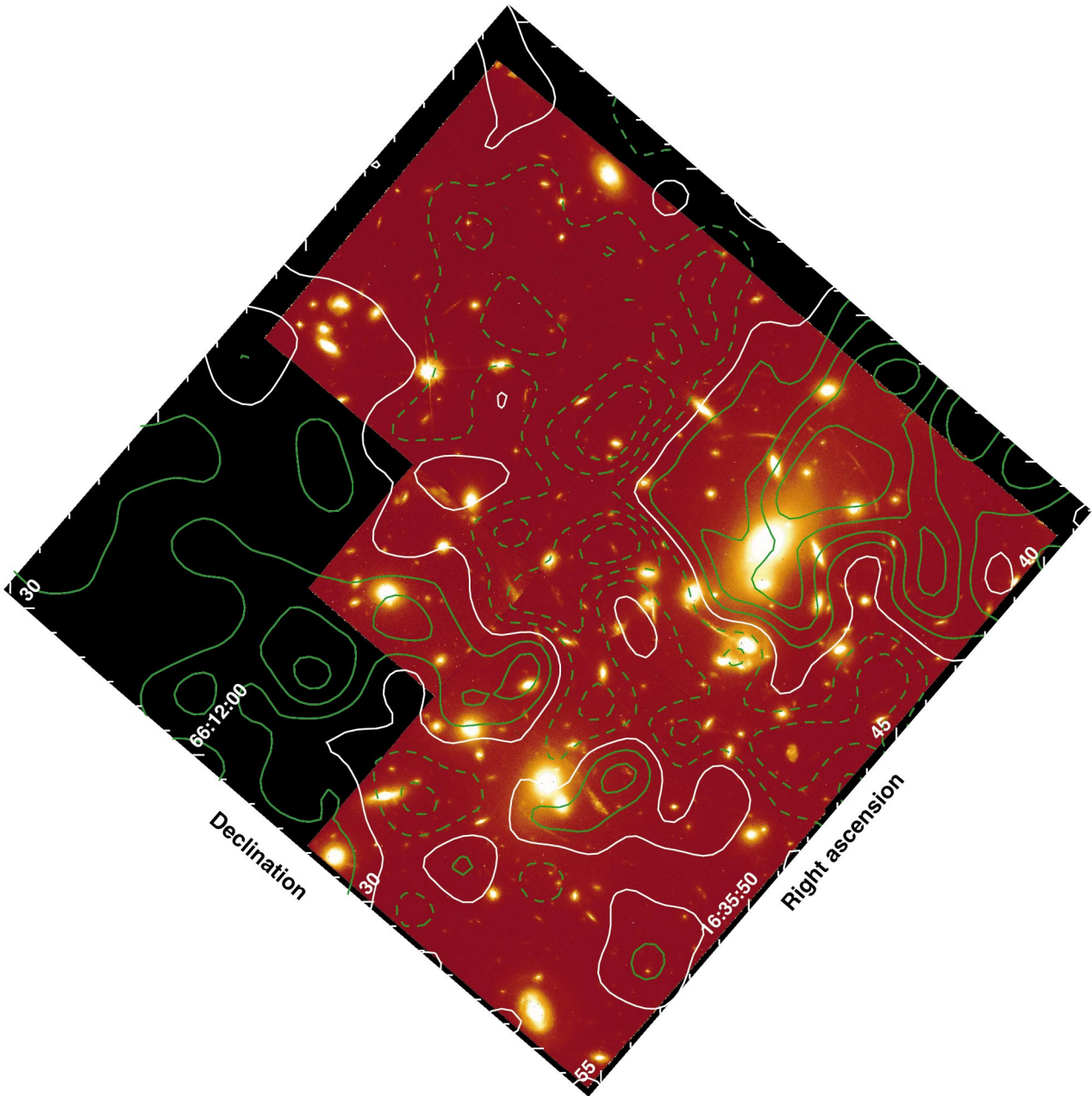


FIG. 3.—Positive (*solid green*), zero (*solid white*), and negative (*dashed green*) contours from the Gaussian-smoothed ($\sigma = 5''$) image of the residuals from the large field beta model fitted to the 0.3–7 keV X-ray surface brightness overlaid on the *HST* mosaic optical image of the core of A2218. The lowest contour is -0.165 counts arcsec $^{-2}$, and the contours increase linearly in increments of 0.041 counts arcsec $^{-2}$.

sion to the north and west of the dominant galaxy. A less prominent excess is also found near the second brightest elliptical galaxy.

The images of Figures 2 and 3 suggest variations in the X-ray emission along the direction of the mass elongation of the cluster. In order to investigate this variation more quantitatively, we choose a set of rectangular ($252'' \times 4''.92$) grids aligned perpendicular to a line that contains the mean (beta model) centroid of emission and lies along the direction of the mass elongation (see Fig. 4). In the top two panels of Figure 5 we show the surface brightness profile for each of the energy bands (soft, hard, and broad) determined by projecting the photon counts in each grid box onto the axis line. Errors are \sqrt{N} , where N is the number of counts in the grid box. The origin is set at the mean X-ray emission center

determined from averaging over the beta models listed in Table 2 ($\alpha = 16^h35^m52^s.3$, $\delta = +66^\circ12'35''.2$). Positive angles are to the north and west. For reference, the location of the cD galaxy and second brightest elliptical galaxy, projected onto the line, are at $r = +20''.4$ and $r = -47''.1$, respectively. We denote these positions on Figure 5 by solid and dotted vertical lines, respectively. The data are not background-subtracted. The mean background levels expected per box are 17.7, 7.9, and 9.9 counts for the broad, soft, and hard energy bands, respectively. We also plot (*solid curve*) the prediction of the large-field beta model plus constant background on the grid for the broad (0.3–7 keV) energy band and show its residuals in the third panel of Figure 5. Although the large aperture beta model plus constant background provides a reasonable description of the broadband

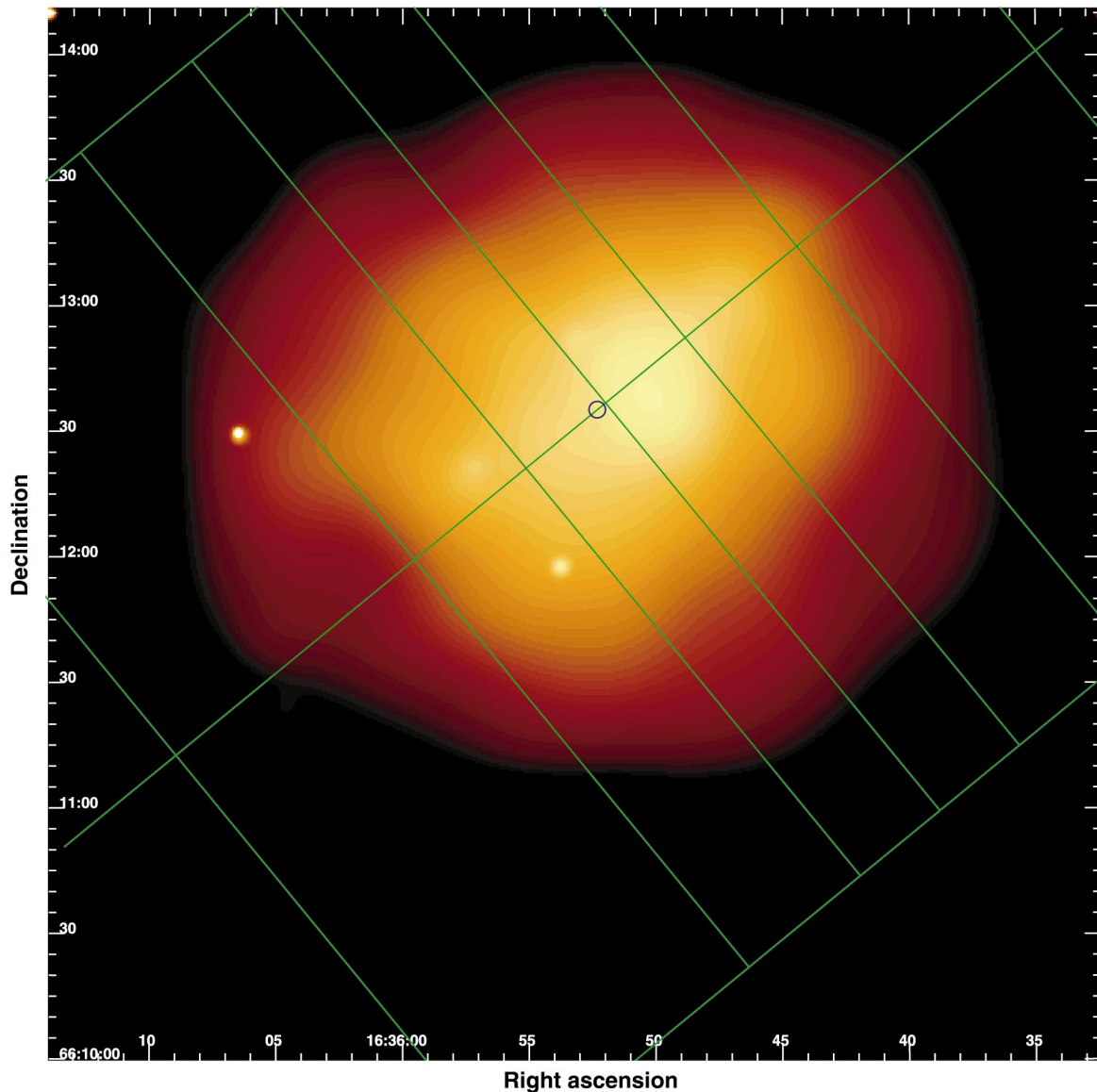


FIG. 4.—Broadband (0.3–7 keV) adaptively smoothed image of the inner 4.2×4.2 core of the cluster overlaid with the axis line and temperature grid used in Fig. 5. The mean beta model centroid ($r = 0$ in Fig. 5) is denoted by a circle.

X-ray surface brightness given the statistical accuracy of our data, weak deviations suggesting a possible bimodal structure and dynamical activity within the core are present within $100''$ of the beta model center. The soft band, with the exception of a possible excess near the location of the second brightest elliptical, seems to mirror closely the broadband distribution. The hard band data are, however, skewed to positive r with a broad, nearly flat peak that extends over and beyond the location of the cD galaxy. We note that the possible excess of photons observed in the soft band at $r \sim -45''$ lies near the location of the second mass concentration found by AbdelSalam et al. (1998) in their nonparametric fit to the gravitational lensing data.

In the bottom panel of Figure 5 we plot the temperature profile across the core along the same axis. However, for such short exposures, we do not have enough photon counts per grid box to extract a reliable spectrum. Thus, we group the grids such that each grouping has ~ 3000 total counts in the combined image data before extracting the spectra separately. We display these grid groups and the

axis line overlaid on the adaptively smoothed broadband image of the cluster core in Figure 4 for reference. We again jointly fit the spectra from the two observations with a single-temperature Raymond-Smith plasma model fixing the absorption column at its Galactic value ($3 \times 10^{20} \text{ cm}^{-2}$) and the metal abundance at 0.2 determined from the mean spectrum for the cluster. The temperature profile shows clear, azimuthally asymmetric variation along the axis of the mass elongation. However, the temperature variations are mild. The temperature remains close to its mean cluster value ($kT \sim 7 \text{ keV}$) south and east of the emission center (for $-140'' \lesssim r \lesssim 0''$). It rises to $kT = 8.70^{+2.1}_{-1.5} \text{ keV}$ across the region containing the flat hard band emission peak ($0 \lesssim r \lesssim 60''$) and then falls abruptly to $kT = 5.5^{+1.2}_{-0.9} \text{ keV}$, well below the cluster mean temperature, for $60'' \lesssim r \lesssim 140''$. Uncertainties are all 90% confidence limits.

It is natural to ask whether the data are consistent with shocks in the gas expected when two merging substructures collide. We can crudely estimate the compression factor ρ_1/ρ_0 of the gas across such a shock front using the X-ray

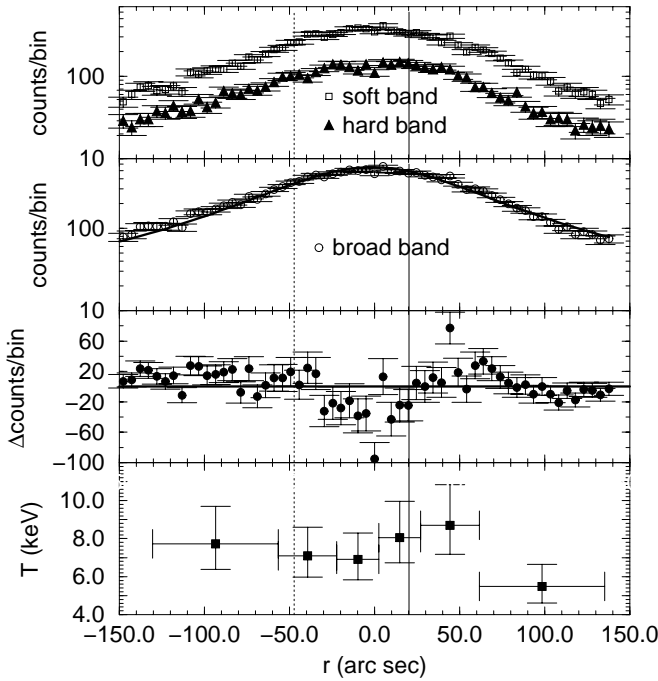


FIG. 5.—*First panel*: Surface brightness profiles for the soft band (0.3–2 keV; open squares) and hard band (2–7 keV; filled triangles) projected on the axis shown in Fig. 4 with the origin placed at the mean X-ray distribution centroid. Error bars are \sqrt{N} Poisson errors only, and the bin width along the line is 4''.92. Vertical solid (dotted) lines denote the projected positions of the dominant cD (second brightest elliptical) galaxies. *Second panel*: Surface brightness profile for the broadband (0.3–7 keV) using the same coordinate conventions as in the first panel. The solid line is the best-fit beta model for the broadband data. *Third panel*: Residuals between the broadband surface brightness distribution and the large field beta model projected onto the symmetry line. Errors are \sqrt{N} only. *Fourth panel*: Temperature profile through the core. The error bars in position denote the bin width along the symmetry line. Temperature errors are 90% CL from the fit.

brightness data:

$$\frac{\rho_1}{\rho_0} \approx \left(\frac{S_{X1}}{S_{X0}} \right)^{1/2}, \quad (3)$$

where $\rho_1(\rho_0)$ are the downstream (upstream) gas densities and $S_{X1}(S_{X0})$ are the corresponding X-ray photon counts per bin. Under the assumptions of an ideal gas and adiabaticity, the compression ratio, temperature ratio, and gas velocities across the shock are then simply related through the shock jump conditions (Mihalas & Mihalas 1984, pp. 220–239). Let $x = \rho_0/\rho_1$ denote the inverse of the compression factor. Then the downstream to upstream temperature ratio is

$$\frac{T_1}{T_0} = \frac{(\gamma + 1)x - (\gamma - 1)x^2}{(\gamma + 1)x - (\gamma - 1)}, \quad (4)$$

where $\gamma = 5/3$ is the adiabatic index. In the rest frame of the shock the downstream-to-upstream velocity ratio is $u_1/u_0 = x$, while the shock velocity difference is

$$u_0 - u_1 = \left[\frac{kT_0}{\mu m_p} (1 - x) \left(\frac{T_1}{xT_0} - 1 \right) \right]^{1/2}, \quad (5)$$

where k is Boltzmann's constant, $\mu = 0.6$ is the mean molecular mass of the gas (assumed fully ionized), and m_p is the proton mass. Upstream (downstream) Mach numbers

$m_0(m_1)$ are given by

$$m_0^2 = 1 + \frac{(\gamma + 1)}{2\gamma} \left(\frac{T_1}{xT_0} - 1 \right)$$

$$\text{and } m_1^2 = 1 - \frac{(\gamma + 1)}{2\gamma} \left(1 - \frac{T_0 x}{T_1} \right). \quad (6)$$

The most striking feature in Figure 5 is the asymmetric temperature drop observed for $r \geq 60''$. If this were to be interpreted as the upstream edge of a shock located at $r \approx 60''$, the measured temperature ratio $T_1/T_0 = 1.59$ with equation (4) would imply a compression factor ≈ 1.8 . Such a shock would not be strong with upstream (downstream) gas velocities and Mach numbers of 1920 (1050) km s⁻¹ and 1.59 (0.69), respectively. This is in agreement with simulations that predict Mach numbers for shocks from merger events in clusters to be $\lesssim 3$ (Sarazin 2002 and references therein). However, from equation (3) we should also expect to see an X-ray surface brightness discontinuity $S_{X1}/S_{X0} \approx 3.3$ on the high-temperature side of the shock ($r \lesssim 60''$) that is clearly not in the data. Furthermore, although the fractional changes in entropy and pressure are formally positive across the discontinuity ($0.6^{+0.9}_{-0.6}$ and $0.6^{+1.0}_{-0.6}$, respectively), the errors are so large that we cannot rule out the possibility that these properties are actually continuous. Thus, unless the required enhancement in X-ray surface brightness has been washed out because of projection effects, this temperature change is unlikely to be associated with a shock. There does appear to be a possible ($\sim 1 \sigma$) excess of X-ray photons over that predicted by the beta model fit in three consecutive bins ($60'' < r < 70''$) in the cold region. This could represent slightly denser, unmixed gas from the primary cluster core. An alternative explanation could be that we are seeing evidence of a cold cloud or cold gas inflowing along a filament prior to merger.

Another statistically weak feature that might be correlated with a shock is the sharp X-ray brightness enhancement seen at $r \approx 45''$. If this feature is a shock and we ignore possible projection effects, the brightness discontinuity and equation (3) imply a compression factor of 1.12, a temperature ratio of 1.08, and upstream (downstream) Mach numbers 1.08 (0.93). The $\sim 8\%$ temperature rise expected for such a shock cannot be detected with the current data set, nor can we definitively distinguish between a weak shock and a possible contact discontinuity at this location.

Thus, our data show no evidence for strong shocks in the cluster core. However, much better temperature data are needed before the presence (or absence) of weak shocks can be definitively determined.

3.3. Projected X-Ray Mass Distribution

One of the most interesting unresolved issues surrounding A2218 is the discrepancy between the measured mass extracted from X-ray data (assuming hydrostatic equilibrium) and that determined from the gravitationally lensed arcs and arclets. Although our data suggest that A2218 is not fully relaxed, it is still useful to follow the usual X-ray mass analysis prescription for the cluster in order to quantify the significance of the cluster's departure from the standard assumptions. Since the large-field, broadband, spherical beta model seems a reasonable description of the surface brightness distribution for the cluster on large scales, we use it and equations (1) and (2) to infer the gas density distribution. However, since the temperature varia-

tion across the core appears azimuthally asymmetric, we do not fit the temperature distribution with a radial profile. Instead we assume isothermality and bracket the mass estimate allowed by our data by using both the mean cluster value $kT = 6.9$ keV, determined from the large aperture spectrum, and $kT = 10.8$ keV, the 90% upper limit to the maximum temperature found from our more detailed analysis of the core. We note that the region of high temperature corresponds to the region containing the brightest gravitationally lensed arcs. However, we do not see gas temperatures as high as those proposed by Cannon et al. (1999) to resolve the discrepancy between the lensing and X-ray mass estimates for this region. Interestingly, Figure 3 shows that there is excess luminosity, implying excess mass, in this region over that predicted by the mean beta model. However, there are too few photon counts in the beta model residuals (see Fig. 5) to constrain a two-component model in this region.

An added complication to the X-ray mass analysis is the fact that most lensing analyses measure the total projected mass within a critical radius b centered on the dominant cD galaxy, while one of the main results of this work is that the center of the cluster gas density distribution is offset from the cD galaxy by $\sim 22''$. We take this offset into account when integrating the total mass within concentric cylinders of radius b centered on the cD galaxy. Assuming that the gas is isothermal and in hydrostatic equilibrium, the total mass density ρ_{tot} is determined from the gas density ρ_g by

$$\rho_{\text{tot}} = \frac{kT}{4\pi G \mu m_p} \nabla^2 \ln \rho_g^{-1}, \quad (7)$$

where k is Boltzmann's constant, T is the gas temperature, $\mu = 0.6$ is the mean molecular mass for the ionized gas, m_p is the proton mass, and G is the gravitational constant. The total projected mass $M(<b)$ within the critical radius b is then found by integrating equation (7) over the volume of the cylinder of radius b , centered on the cD galaxy. As noted by Allen (1998) in a similar analysis of *ROSAT* data, the displacement of the gas mass center from the lensing mass center results in a lower projected mass than would otherwise have been determined from the given beta model had the lensing and gas mass centers coincided.

In Figure 6 we compare the projected total mass $M(<b)$ within a radius b of the cD galaxy obtained from our data for $kT = 6.9$ keV (solid line) and $kT = 10.8$ keV (dashed line) with $M(<b)$ obtained from strong lensing analyses (Loeb

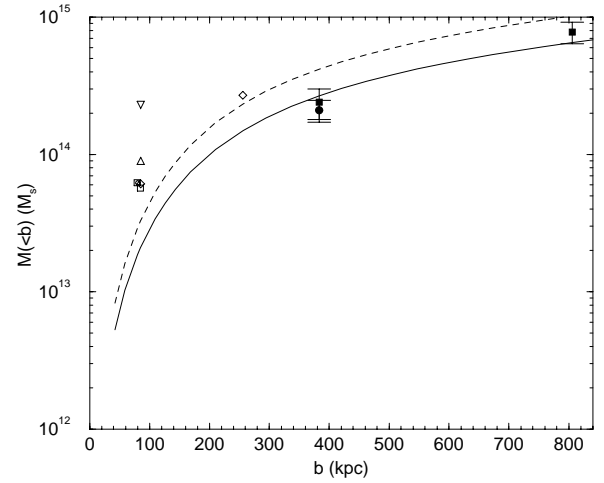


FIG. 6.—Projected total X-ray mass as a function of radial distance b from the dominant cD galaxy using an isothermal spherical beta model with temperatures $kT = 6.9$ keV (solid line) and $kT = 10.8$ keV (dashed line) and the SCDM cosmology ($\Omega_m = 1$, $H_0 = 50 \text{ km s}^{-1} \text{ Mpc}^{-1}$). The strong lensing results are from Loeb & Mao 1994 (open circle), Kneib et al. 1995 (open diamonds), and Allen 1998 (open squares). Weak lensing results are from Squires et al. 1996 (filled squares) and Smail et al. 1997 (filled circle). The up (down) triangle are the minimum (maximum) mass reconstructions of AbdelSalam et al. 1998 using both weak and strong lensing constraints.

& Mao 1994; Kneib et al. 1995; Allen 1998), weak lensing analyses (Squires et al. 1996; Smail et al. 1997), and the minimum and maximum mass models from a nonparametric reconstruction method (AbdelSalam et al. 1998) that uses both strong and weak lensing data. Note that the scatter in the lensing results at small radii is due to the nonuniqueness of the mass model used in the various analyses. Furthermore, the weak lensing results at large radii should be considered lower bounds on the enclosed mass. Squires et al. (1996) estimated that residual cluster mass in their selected reference annulus would increase their measurement of the weak lensing mass within $r \lesssim 400 h^{-1}$ by 20%–60% depending on the assumed cluster mass model. However, since this correction factor is so highly model-dependent, we show only their uncorrected measurements in Figure 6 and Table 4. We present our mass results in the SCDM ($\Omega_0 = 1$, $\Omega_\Lambda = 0$, $h = 0.5$) cosmology for direct comparison with previous work. The results for the Λ CDM model that we have heretofore assumed can be

TABLE 4
LENSING-TO-X-RAY MASS RATIOS

Lensing Reference	b (arcsec)	b (kpc)	M_{lens} ($\times 10^{14} M_\odot$)	M_{Xc} ($\times 10^{14} M_\odot$)	M_{Xh} ($\times 10^{14} M_\odot$)	M_{lens}/M_{Xc}	M_{lens}/M_{Xh}
Loeb & Mao 1994.....	20.8	79.8	0.64	0.19	0.29	3.4	2.2
Allen 1998	20.7	79.4	0.62	0.19	0.29	3.4	2.1
Kneib et al. 1995	22.1	84.8	0.61	0.21	0.32	2.9	1.9
Allen 1998	22.1	84.8	0.57	0.21	0.32	2.7	1.8
AbdelSalam et al. 1998.....	22.1	84.8	0.9	0.21	0.32	4.3	2.8
Kneib et al. 1995	66.7	256	2.7	1.49	2.33	1.8	1.2
Squires et al. 1996	99.8	383	2.4 ± 0.6	2.67	4.18	0.9	0.6
Smail et al. 1997	99.8	383	2.1 ± 0.38	2.67	4.18	0.8	0.5
Squires et al. 1996	210	806	7.8 ± 1.4	6.52	10.20	1.2	0.8

NOTE.—The first six entries are strong lensing results, while the last three are lower bounds on the mass from weak lensing analyses. M_{Xc} and M_{Xh} are the X-ray masses for $kT = 6.9$ keV and the upper bound $kT = 10.8$ keV, respectively, assuming an $\Omega_m = 1$, $\Omega_\Lambda = 0$, $h = 0.5$ cosmology. The minimum mass model result is used from AbdelSalam et al. 1998.

obtained by multiplying the mass by a factor 0.83, the ratio of the Λ CDM ($h = 0.65$) to SCDM ($h = 0.5$) distance scales.

For clusters such as A2218 where the mass structure is multi-peaked and may not follow the light, the uncertainties in the lensing mass determination can be large. However, all of the lensing results for the total projected mass within the critical radii of the brightest arcs ($b < 85$ kpc) lie well above the total mass determined from the X-ray data. In Table 4 we list the ratio of the lensing to X-ray-projected masses within selected radii b centered on the dominant cD galaxy. The agreement between the weak lensing mass and the X-ray mass determined in our simple isothermal ($kT = 6.9$ keV) spherical model is excellent at larger radii ($b \gtrsim 200 h^{-1}$ kpc). However, the X-ray and lensing mass estimates become more discrepant as b decreases even if we use in our model the 90% upper limit on the highest temperature measured for the core region as characteristic of all the mass in the projection cylinder. This latter estimate may be interpreted as a conservative upper bound on the projected X-ray mass since it not only represents the 90% upper bound on the maximum temperature measured in the core, but by using this temperature for all of the gas in the projection cylinder, it also overestimates the contribution of the cooler gas at large cluster radii.

4. DISCUSSION

The results discussed above in § 3 strongly support the hypothesis that A2218 is not fully relaxed, especially in its core. Our first indication of dynamical activity within the cluster is the displacement of the X-ray centroid from that of the dominant cD galaxy. Numerical simulations demonstrate that complicated multi-peaked differences between the total mass, light, and X-ray emission in clusters signal recent or ongoing merger activity (see, e.g., Bryan 1996; Evrard, Metzler, & Navarro 1996; Roettiger, Stone, & Mushotzky 1998). Roettiger et al. (1998) showed that ram pressure induced by a slightly off-axis collision between a massive subcluster and the primary mass concentration (2.5 times more massive) is sufficient to displace the gas distribution from that of the total mass and light. Furthermore, the subcluster's dark matter halo can maintain its identity for several additional core crossings. On each encounter it continues to disturb the cluster core such that the relaxation of the cluster back to hydrostatic equilibrium is slow. In related numerical studies, Gomez et al. (2002) found similar patterns of gas evolution in head-on collisions between a primary cluster and infalling subcluster with a 16:1 mass ratio between the components, provided that the gas content of the subcluster was sufficiently high. The ratio of the primary to secondary mass concentrations in A2218, as modeled through lensing analyses (Kneib et al. 1996), is $\sim 12:1$, intermediate between these extremes. Thus, we expect the general features of such a collision to be qualitatively similar.

On closer examination of the cluster core we can probe in more detail the dynamics of the proposed merger. The isophotal twisting and general elongation of the contours in Figure 2 along the line containing the two major mass concentrations as well as the distortions perpendicular to this axis can both be understood within this scenario. Gas dragged outward by the subcluster potential from the region surrounding the primary mass concentration causes the general elongation along the merger axis. In simulations of mergers with 16:1 (2.5:1) mass ratios between the com-

ponents, this elongation of the brightness (and thus density) distribution caused by the gas response to the elongated gravitational potential persists for at least 1 Gyr (3 Gyr) after the initial core crossing (Gomez et al. 2002; Roettiger et al. 1998). Bulk flows generated by the initial merger event produce a global circulation of the gas. Gas is driven perpendicular to the merger axis in places distorting the X-ray contours along the direction of these flows (Roettiger et al. 1998). The departures from a simple isothermal beta model displayed in the pattern of residuals seen in Figure 3 can be interpreted as a consequence of these gas flows. Within our merging hypothesis the lower density regions (negative residuals with respect to the mean beta model) would again correspond to regions where the gas has been swept outward along the direction of the bulk velocity flows. The steep gradient represents a region of compression of the gas near and beyond the dominant galaxy. This could be caused partly by the compression of the gas due to the shock produced in the initial collision but more importantly by adiabatic compression of the gas when the global bulk circulation of the gas meets itself as the merger evolves (Roettiger et al. 1998). If so, this region where the gas is compressed should correspond to a region of higher temperature due primarily to adiabatic heating of the gas when the velocity flows meet. This is consistent with the temperature profile shown in Figure 5 and would also account for the displacement of the peak in the hard emission seen in Figure 2. Such velocity flows may already have been measured in the Centaurus Cluster using *ASCA* data (Dupke & Bregman 2001). The excess emission near the second brightest elliptical galaxy in Figure 3 could be due to gas dragged out of the primary core by the gravitational potential of the subcluster.

The brightness distribution and mild asymmetric temperature variations in Figure 5, although broadly averaged, provide important clues about the evolutionary stage of the merger. We see no evidence for the bow shock and associated large temperature and brightness discontinuities expected in the early stages of a merger just after the primary collision. Rather, the data are qualitatively consistent with simulations of a slightly off-axis merger ~ 1 – 2 Gyr after the initial interaction (Roettiger et al. 1998; Roettiger, Stone, & Burns 1999). In such a picture we expect the bow shock to be mildly supersonic so that it will have migrated out of our $\sim 1 h^{-1}$ Mpc field in $\lesssim 1$ Gyr, the sound crossing time for this field. Regions of the gas have been adiabatically compressed and heated by the bulk velocities established in the early stages of the merger. The subcluster dark matter core has survived several additional core crossings and with each crossing “stirs” the intracluster gas breaking the large-scale velocity flows into smaller scale turbulent eddies. However, mixing of the gas (and the approach to hydrostatic equilibrium) is slow. Simulations show that large cold regions of gas may still be present several gigayears after the first collision, which could explain the sudden drop in temperature north and west of the cD galaxy and the azimuthally asymmetric pattern of hot and cold regions found in our map. Furthermore, by this time the extremes in temperature have been mitigated such that when azimuthally averaged the cluster would appear largely isothermal, also in agreement with our data (Markevitch et al. 2001).

Although agreement is good between the X-ray and lensing estimates of the total projected mass at large radii

($\geq 200 h^{-1}$ kpc), indicating that when averaged over large scales the cluster appears largely isothermal and in hydrostatic equilibrium, the lensing analyses at the smallest scales ($\sim 40 h^{-1}$ kpc) are consistently a factor 2–3 larger than the X-ray mass estimates. We note, following various authors (Evrard 1990; Loeb & Mao 1994; Miralda-Escude & Babul 1995; Bartelmann & Steinmetz 1996), that two distinct phenomena associated with merging exacerbate the measured differences between the strong lensing and X-ray estimates in the cluster core. First, the departure from hydrostatic equilibrium in the core signaled by the presence of nonthermal pressures due to bulk plasma flows, turbulence, or the merger-induced amplification of magnetic fields causes the X-ray method, which presumes hydrostatic equilibrium, to underestimate the mass. Second, significant substructure along the line of sight is more likely in dynamically active clusters and, if present, will cause the lensing technique to overestimate the mass. We consider each of these phenomena in turn.

Because of the limited resolution of current numerical simulations (Roettiger et al. 1998, 1999), it is difficult to determine from them whether nonthermal pressures alone can be as large as required by our data. These simulations do show, however, that both nonthermal kinetic pressures and magnetic field amplification can be significant during the intermediate stages of the merger (~ 1 – 2 Gyr after the primary encounter) and that both effects tend to increase when the simulations are able to resolve smaller scales. Roettiger et al. (1998) found that when averaging over spheres of $0.4 h^{-1}$ Mpc the nonthermal kinetic pressure still reached values 40% of the thermal pressure at ~ 2 Gyr after the primary encounter, twice that obtained at the same epoch for a sphere whose radius was 4 times larger ($r = 1.5 h^{-1}$ Mpc). They concluded that neglect of the dynamical pressure component during the first ~ 2 Gyr after a major merger will cause a significant underestimate of cluster mass and that the underestimate will be most severe when the analysis is restricted to the central regions of the cluster. Thus, it is possible that if we average over regions another order of magnitude smaller than those in the simulation, such as the $\sim 40 h^{-1}$ kpc critical radius of the brightest lensed arc, that the dynamical pressure due to bulk and turbulent flows could reach values comparable to the thermal pressure of the gas in that region. We should expect, as seen in our analysis, that agreement between the X-ray mass and lensing mass estimates improve as we move to larger radii.

Roettiger et al. (1999) also show that it is at this intermediate stage of the merger evolution when the bulk velocity flows become broken up into smaller scale turbulent eddies and amplification of localized magnetic fields is maximal. They find with their limited resolution (~ 12.5 kpc) that the magnetic energy on small scales is amplified by a factor ~ 26 over that in a nonmerging cluster and speculate that with better resolution simulations, the amplification of magnetic energies due to turbulent eddies on yet smaller scales could be much greater. New, high-resolution observations of several dynamically active clusters by *Chandra* (Vikhlinin, Markevitch, & Murray 2001b; Sarazin 2002) indicate that scales on the order of a few kiloparsecs are likely to be dynamically important, scales roughly an order of magnitude smaller than the highest resolution simulations by Roettiger et al. (1998, 1999). For example, in A3667 cold fronts with sharp edges were found where dramatic

changes in temperature and X-ray surface brightness occur over ~ 2 kpc scales. The suppression of thermal conduction implied by the *Chandra* data for A3667 argues for significant amplification of the magnetic field to strengths $\sim 10 \mu\text{G}$ over kiloparsec scales, translating into modest (but still significant) nonthermal magnetic pressures between 10% and 20% of thermal at the edge of the cold front (Vikhlinin, Markevitch, & Murray 2001a). Measures of Faraday rotation in a sample of fully relaxed clusters, i.e., those with no strong radio sources, cooling flows, or signs of recent merging activity, by Clarke, Kronberg, & Böhringer (2001) imply magnetic field strengths $\sim 4 \mu\text{G}$ in a tangled magnetic field model with constant coherence length of 15 kpc and $H_0 = 50 \text{ km s}^{-1} \text{ Mpc}^{-1}$. They argue that magnetic fields could reach values as high as $\sim 8 \mu\text{G}$ for kiloparsec coherence lengths near the cluster cores.

The presence of significant magnetic fields in the inner region of A2218 is consistent with VLA data that show a weak, centrally located radio halo in the cluster core (Moffet & Birkinshaw 1989; Giovannini, Tordi, & Feretti 1999). Such radio halos are usually found in clusters that show evidence of recent merging activity (Buote 2001; Buote & Tsai 1996). The relativistic electrons responsible for the low-frequency (1.4 GHz) radio emission observed in these halos are thought to be initially accelerated by the shocks produced in the initial stages of a major merger. These electrons can then be reaccelerated by the subsequent turbulent eddies produced in the gas during the intermediate stage of the merger evolution after the shock has traveled out of the core (Sarazin 2000, 2002). The weakness of the radio halo found in A2218 may be a consequence of the fact that we are observing the cluster at such an intermediate stage, ≥ 1 Gyr after the primary collision. However, if we were to assume equipartition between the thermal, kinetic, and magnetic energies in the innermost core of A2218, the data would require an average magnetic field strength within the critical radius of the brightest arc of $\geq 50 \mu\text{G}$ to reconcile the lensing and X-ray mass estimates. This would require amplification of the average magnetic field energy in this region due to turbulent small-scale eddies by factors ≥ 40 over those expected near the cores of fully relaxed clusters and a factor ≥ 2 larger than found in existing simulations (Roettiger et al. 1999). Thus, while it is likely that kinetic and magnetic pressures are important during this stage of the merger evolution, we need both better data and higher resolution simulations to determine whether quantitative agreement is possible solely because of the presence of these nonthermal pressures.

Another possible contributor to the difference in lensing and X-ray masses in A2218 is the chance alignment of substructure along the line of sight. Bartelmann & Steinmetz (1996) argued from simulations that ongoing merging activity, as evidenced by substructure in clusters, significantly enhances a cluster's ability to form multiple arc systems. This is consistent with our conclusion that A2218 is dynamically active. They further found that in the few simulated clusters in which the discrepancy between the projected lensing and X-ray masses was large (up to factors ~ 2 , as is the case for our data) that the radial velocity distributions were bimodal, indicating the infall of substructure along the line of sight. Studies of both the optical (Zabludoff & Mulchaey 1998) and X-ray (Mulchaey & Zabludoff 1998) properties of a sample of nearby galaxy groups found that groups with detectable X-ray emission behaved very much

like low-mass galaxy clusters. The X-ray-emitting groups in this sample are bound systems with characteristic temperatures ~ 1 keV, a median harmonic radius $r_h = 0.82$ Mpc, and virial masses in the range $(0.8\text{--}2) \times 10^{14} M_\odot$ (assuming $\Omega_0 = 1$, $h = 0.5$). Zabludoff & Mulchaey argue that the harmonic radius is a good approximation to r_{500} , where dynamical equilibrium is achieved for systems at this temperature. The virial mass is large compared to both the mass contained in X-ray gas ($\sim 6 \times 10^{12} M_\odot$) and in galaxies ($\sim 2 \times 10^{13} M_\odot$) and is distributed in a large, common halo with a bright elliptical galaxy located at its center. The X-ray emission consists of two components, a compact (core radius ~ 40 kpc) soft (0.7–0.9 keV) component thought to be associated with the central elliptical galaxy and a fainter, extended component (core radius ~ 200 kpc) that is most likely emission from the intragroup gas. These groups thus serve as useful models for the subclusters expected to participate in merging in a rich cluster environment.

If we assume a singular isothermal density profile ($\rho \propto r^{-2}$) for such a group infalling along the line of sight, the maximum contribution of the group to the projected total mass within the critical radius b can be no larger than $M(<b) < (\pi/2)(b/r_v)M_v$, where M_v and r_v are the virial mass and radius, respectively. For the brightest lensed arc of A2218, $b = 80$ kpc such that $b/r_v \sim 0.1$. Thus, an infalling group with mass in the range characteristic of the Zabludoff & Mulchaey sample could account for as much as 30%–70% of the discrepancy between the lensing and X-ray-projected mass estimates within the brightest arc. Changing the density profile of the group to a Navarro-Frenk-White or Moore profile reduces the group contribution since each of these profiles is less concentrated ($\rho \propto r^{-1}$ or $\rho \propto r^{-1.5}$, respectively) in the core than the singular isothermal profile assumed above. X-ray emission from such an intervening group would most likely be observable in our *Chandra* data. The X-ray signature for such a group would be enhanced soft emission, with a scale of ~ 40 kpc ($\sim 10''$), coincident with a bright elliptical galaxy, and with no corresponding feature in the hard band. It is interesting to note that the peak of the soft emission in our data is nearly coincident with the elliptical galaxy 1662 from Ziegler et al. (2001). Thus, an intervening group could possibly account for the displacement of the hard and soft band emissions seen in our data. However, if galaxy 1662 is interpreted as the center of this group, as the X-ray emissions might imply, the $\sim 18''$ offset of the group center from the dominant cD galaxy would also reduce the above estimate of the group's contribution to the projected mass.

Thus, we conclude that recent merging within dynamically active clusters disrupts hydrostatic equilibrium in the cluster core producing significant nonthermal pressures there so that the standard (thermal hydrostatic equilibrium) X-ray mass analyses tend to underestimate the cluster mass. In addition, the presence of substructure in these clusters increases the likelihood that the projection of an infalling group along the line of sight will cause the strong lensing mass to be an overestimate, thus enhancing the measured discrepancy. We find that the contribution from an intervening galaxy group along the line of sight may be significant in A2218. However, it probably cannot by itself reconcile the discrepancy between the lensing and X-ray-projected mass estimates within the $40 h^{-1}$ kpc radius of the brightest arc. Our data suggest that a full explanation of the

lensing-to-X-ray mass discrepancy in A2218 most likely requires a somewhat higher thermal pressure because of the hotter temperature of the gas in the core region, the presence of significant nonthermal pressure support because of turbulent velocities and perhaps amplified magnetic fields, and possibly the chance projection of galaxy group-sized substructure along the line of sight. These effects are expected to be important at an intermediate stage of a major merger ($\gtrsim 1$ Gyr after the primary collision) when the return to hydrostatic equilibrium in the central region of the cluster has been delayed by additional interactions with the subcluster dark matter core. Better quantitative tests of this picture will be provided by deeper X-ray imaging, plasma velocity maps obtained from high-resolution X-ray spectroscopy, and better simulations that take into account a range of subcluster-to-primary cluster mass ratios and collision parameters with sufficient resolution to model physical processes on the kiloparsec scales now shown by *Chandra* observations to be dynamically important.

5. SUMMARY

In this paper we presented the results from two short observations (combined exposure of ~ 17 ks) of galaxy cluster A2218 taken on 1999 October 19 using the ACIS-I detector on board the *Chandra X-Ray Observatory*. In summary, we found the following:

1. Using a Raymond-Smith single-temperature plasma model corrected for galactic absorption on data within a $5'.1$ (~ 1 Mpc) radius circular aperture of the cluster core, we find a mean cluster temperature of $kT = 6.9 \pm 0.5$ keV, metallicity of 0.20 ± 0.13 , and rest-frame 2–10 keV luminosity of 6.2×10^{44} ergs s^{-1} in the Λ CDM, $H_0 = 65$ km s^{-1} Mpc $^{-1}$ cosmology, in agreement with previous measurements.

2. The broadband (0.3–7 keV) X-ray brightness distribution within $4'.2$ of the cluster core is well fitted by a simple spherical beta model with core radius $66''.4$ ($138 h^{-1}$ kpc), index $\beta = 0.70$, and normalization $S_{x0} = 0.967$ counts $arcsec^{-2}$. However, the centroid of the distribution is displaced by $\sim 22''$ to the east and south of the dominant cD galaxy along the direction of the primary mass concentration found by AbdelSalam et al. (1998) and similar to displacements found in analyses of *ROSAT* data by Markevitch (1997) and Allen (1998). If we relax the assumption of spherical symmetry, we find the cluster ellipticity is 0.179, close to spherical, with no significant change in β or the location of the emission centroid.

3. Examination of the central $2'$ of the cluster core reveals that the peaks of the soft (0.3–2 keV) and hard (2–7 keV) X-ray emission are displaced from each other (and the emission centroid) along the direction of the mass elongation of the cluster. Such multi-peaked behavior suggests ongoing merging activity within the core.

4. The gas temperature profile, projected onto a line extending along the direction of the mass elongation, shows a temperature increase in the region surrounding the dominant cD galaxy and asymmetric behavior with respect to the emission centroid. Temperatures are close to the cluster mean temperature out to $2'$ to the south and east of the emission centroid, while the temperature falls sharply $1'$ – $2'$ to the north and west.

5. We see no evidence for strong shocks within the cluster core. However, weak shocks cannot be ruled out by

our data, and there may be weak evidence for cold clouds or trapped gas denoting a complicated core structure.

6. The discrepancy of a factor of 2–3 in the lensing-to-X-ray mass ratio persists for the smallest critical radii $b \sim 40 h^{-1} \text{ kpc}$ ($21''$ – $22''$) measured relative to the dominant cD galaxy. Although a chance alignment of substructure along the line of sight could reduce the size of this discrepancy, reconciliation of the lensing and X-ray masses at this critical radius would still require the ratio of nonthermal to thermal pressure to be $\gtrsim 1$. Agreement improves, however, for larger b and becomes good for comparisons between the weak lensing masses and the enclosed projected X-ray mass for critical radii $\gtrsim 200 h^{-1} \text{ kpc}$ ($100''$).

These data, although photon count-limited, clearly suggest that the intracluster gas in the core of A2218 is not in hydrostatic equilibrium. The superb spatial resolution of the *Chandra* satellite now makes it feasible to study the details of the merging processes expected to be responsible for the formation and evolution of galaxy clusters. Our data are qualitatively consistent with the view that we are seeing

the cluster intermediate between the primary collision and its eventual relaxation to hydrostatic equilibrium. Simulations suggest that at this stage of merger evolution gas mixing is incomplete, bulk and turbulent flows are present, and localized magnetic field amplification within the core is maximized. With the longer exposure observations planned for A2218 in the near term, we should be able to make a high-resolution temperature map of the central regions of the cluster to test this hypothesis further. In the future the high-resolution spectroscopy planned for *ASTRO-E2* and *Constellation X* will allow us to map gas velocity flows as well with the hope of finally disentangling the dynamics of these complex processes evolving deep within the cluster core.

This work is supported in part by NASA contracts NAS 8-37716, NAS 8-38252, and 1797-MIT-NA-A-38252. We gratefully thank Leon Van Speybroeck for sharing his data, Lilya Williams for making her mass map available to us, Greg Bryan and Paul Schechter for useful discussions, and John Arabadjis for help with the images.

REFERENCES

- AbdelSalam, H. M., Saha, P., & Williams, L. L. R. 1998, *AJ*, 116, 1541
 Allen, S. W. 1998, *MNRAS*, 296, 392
 Bartelmann, M., & Steinmetz, M. 1996, *MNRAS*, 283, 431
 Bautz, M. W., et al. 1998, *Proc. SPIE*, 3444, 210
 Birkinshaw, M., & Hughes, J. P. 1994, *ApJ*, 420, 33
 Bryan, G. L. 1996, Ph.D. thesis, Univ. Illinois at Urbana-Champaign
 Buote, D. 2001, *ApJ*, 553, L15
 Buote, D. A., & Tsai, J. C. 1996, *ApJ*, 458, 27
 Cannon, D. B., Ponman, T. J., & Hobbs, I. S. 1999, *MNRAS*, 302, 9
 Clarke, T. E., Kronberg, P. P., & Böhringer, H. 2001, *ApJ*, 547, L111
 David, L. P., Slyz, A., Jones, C., Forman, W., Vrtilek, S. D., & Arnaud, K. A. 1993, *ApJ*, 412, 479
 Dobrzycki, A., Ebeling, H., Glotfelty, K., Freeman, P., Damiani, F., Elvis, M., & Calderwood, T. 1999, *Chandra* Detect V1.0 User's Guide (Cambridge: *Chandra* X-Ray Center)
 Dupke, R. A., & Bregman, J. N. 2001, *ApJ*, 547, 705
 Evrard, A. E. 1990, *ApJ*, 363, 349
 Evrard, A. E., Metzler, C. A., & Navarro, J. F. 1996, *ApJ*, 469, 494
 Freeman, P. E., Kashyap, V., Rosner, R., & Lamb, D. Q. 2002, *ApJS*, 138, 185
 Garmire, G. P. et al. 1992, in *AIAA, Space Programs and Technologies Conference* (Paper 92-1473; New York: AIAA)
 Giovannini, G., Tordi, M., & Feretti, L. 1999, *NewA*, 4, 141
 Gomez, P. L., Loken, C., Roettiger, K., & Burns, J. O. 2002, *ApJ*, in press
 Kneib, J. P., Ellis, R. S., Smail, I., Couch, W., & Sharples, R. M. 1996, *ApJ*, 471, 643
 Kneib, J. P., Mellier, Y., Pello, R., Miralda-Escude, J., Le Borgne, J.-F., Böhringer, H., & Picat, J.-P. 1995, *A&A*, 303, 27
 Le Borgne, J. F., Pello, R., & Sanahuja, B. 1992, *A&AS*, 95, 87
 Loeb, A., & Mao, S. 1994, *ApJ*, 435, L109
 Loewenstein, M. 1997, in *X-Ray Imaging and Spectroscopy of Cosmic Plasmas*, ed. F. Makino (Tokyo: Universal Academy), 67
 Makino, N. 1996, *PASJ*, 48, 573
 Markevitch, M. 1997, *ApJ*, 483, L17
 Markevitch, M., Vikhlinin, A., Mazzotta, P., & Van Speybroeck, L. 2001, in *ASP Conf. Ser. 234, X-Ray Astronomy 2000*, ed. R. Giacconi, L. Stella, & S. Serio (San Francisco: ASP)
 Mazzotta, P., Markevitch, M., Vikhlinin, W. R., Forman, L., David, P., & VanSpeybroeck, L. 2001, *ApJ*, 555, 205
 McHardy, I. M., Stewart, G. C., Edge, A. C., Cooke, B., Yamashita, K., & Hatsukade, I. 1990, *MNRAS*, 242, 215
 Mihalas, D., & Mihalas, B. W. 1984, *Foundations of Radiation Hydrodynamics* (Oxford: Oxford Univ. Press)
 Miralda-Escude, J., & Babul, A. 1995, *ApJ*, 449, 18
 Moffet, A. T., & Birkinshaw, M. 1989, *AJ*, 98, 1148
 Monet, D. G. 1998, *BAAS*, 193, 120.03
 Morrison, R., & McCammon, D. 1983, *ApJ*, 270, 119
 Mulchaey, J. S., & Zabludoff, A. I. 1998, *ApJ*, 496, 73
 Mushotzky, R. F., & Loewenstein, M. 1997, *ApJ*, 481, L63
 Natarajan, P., & Kneib, J.-P. 1996, *MNRAS*, 283, 1031
 Pello, R., Le Borgne, J. F., Sanahuja, B., Mathez, G., & Fort, B. 1992, *A&A*, 266, 6
 Prigozhin, G., Kissel, S., Bautz, M., Grant, C., LaMarr, B., Forster, R., Richer, G., & Gamire, G. 2000, *Proc. SPIE*, 4012, 720
 Raymond, J. C., & Smith, B. W. 1977, *ApJS*, 35, 419
 Roettiger, K., Stone, J. M., & Burns, J. O. 1999, *ApJ*, 518, 594
 Roettiger, K., Stone, J. M., & Mushotzky, R. F. 1998, *ApJ*, 493, 62
 Sarazin, C. L. 2000, in *Constructing the Universe with Clusters of Galaxies*, ed. F. Durret & D. Gerbal (Gif-sur-Yvette: Editions Frontières), 34
 ———. 2002, in *Merging Processes in Clusters of Galaxies*, ed. L. Feretti, I. M. Gioia, & G. Giovannini (Dordrecht: Kluwer), in press
 Siddiqui, H. 1995, Ph.D. thesis, Univ. Leicester
 Smail, L., Ellis, R. E., Dressler, A., Couch, W. J., Oemler, A., Sharples, R. M., & Butcher, H. 1997, *ApJ*, 479, 70
 Squires, G., Kaiser, N., Babul, A., Fahlman, G., Woods, D., Neumann, D. M., & Böhringer, H. 1996, *ApJ*, 461, 572
 Sunyaev, R. A., & Zel'dovich, Y. B. 1972, *Comments Astrophys. Space Phys.*, 4, 173
 ———. 1980, *ARA&A*, 18, 537
 Vikhlinin, A., Markevitch, M., & Murray, S. S. 2001a, *ApJ*, 549, L47
 ———. 2001b, *ApJ*, 551, 160
 Zabludoff, A. I., & Mulchaey, J. S. 1998, *ApJ*, 496, 39
 Ziegler, B. L., Bower, R. G., Smail, I., Davies, R. L., & Lee, D. 2001, *MNRAS*, 325, 1571